Dalton Transactions

ROYAL SOCIETY OF CHEMISTRY

PAPER

View Article Online
View Journal | View Issue

Cite this: *Dalton Trans.*, 2025, **54**, 17864

Hydrogen adsorption and dissociation on transition metal anchored $B_{12}N_{12}$ nanocages: insights from density functional theory

Zainab Fareed,[a] Tayyaba Tariq,[b] Shaaban M. Shaaban,[c] Muhammad Yar, *[b] Muhammad Ali Khan, [a] Ajaz Hussain,[a] Khurhsid Ayub, [d] Sehrish Sarfaraz*[d] and Yasser M. Riyad *[e]

The growing worldwide transition to carbon-neutral energy systems requires the development of novel, efficient, and sustainable catalysts for key reactions, including hydrogen dissociation. As hydrogen is increasingly recognised as a clean and scalable energy carrier, the design of cost-effective, noble metal-free single-atom catalysts (SACs) has become a pressing priority. In this study, we employ density functional theory (DFT) to systematically explore a new class of SACs based on transition metal-anchored boron nitride nanocages (**M@$B_{12}N_{12}$**) for the hydrogen dissociation reaction (HDR). To better reflect real reaction environments, H_2 dissociation was studied in water using an implicit solvation model. Interaction energy (E_{int}) analyses confirm the thermodynamic stability of all designed complexes, while **Co@$B_{12}N_{12}$**, **Ni@$B_{12}N_{12}$**, **Fe@$B_{12}N_{12}$**, and **Cr@$B_{12}N_{12}$** have been found to possess very low activation energy (E_a) barriers, 0.14 eV, 0.16 eV, 0.19 eV, and 0.21 eV for H_2 activation, respectively, showing the best catalytic performance. To get insights into the intrinsic activation process, we perform detailed natural bond orbital (NBO), electron density difference (EDD), and quantum theory of atoms in molecules (QTAIM) analyses. Furthermore, reduced density gradient (RDG) and non-covalent interaction (NCI) analyses reveal the presence of both weak van der Waals forces and directional covalent interactions that collectively stabilise transition states and promote efficient H–H bond cleavage. Following the multi-dimensional analysis of the electronic structure, the synergistic mechanism of charge transfer and orbital hybridization observed demonstrates that the **Co@$B_{12}N_{12}$** complex exhibited high efficiency as a SAC with a minimum E_a value of 0.14 eV for hydrogen dissociation. The insights provide useful design guidelines for the next-generation hydrogenation catalysts, which directly leads to the establishment of hydrogen technologies that are scalable in providing clean energy solutions to the world.

Received 1st July 2025,
Accepted 27th October 2025

DOI: 10.1039/d5dt01548k

rsc.li/dalton

Introduction

The swift increase in the global population has driven an unprecedented rise in energy demand. However, this surge contrasts sharply with the rapid depletion of traditional fossil fuel resources.[1] Moreover, the persistent reliance on fossil fuels continues to exacerbate environmental degradation, primarily through the emission of greenhouse gases and other pollutants.[2] In light of these dual challenges, energy scarcity and environmental deterioration, there is a pressing need to shift towards cleaner and more sustainable energy solutions. Among the various alternatives, hydrogen emerges as a particularly attractive candidate.[3] It offers high energy density and can be synthesized from renewable resources, and its use results in water as the sole byproduct, thereby minimizing environmental harm.[4] Furthermore, hydrogen demonstrates remarkable energy conversion efficiency, making it especially promising for transportation sectors.[5] Collectively, these attributes establish hydrogen as a critical player in the transition towards a sustainable and environmentally responsible energy future.[6] Hydrogen dissociation involves the cleavage of molecular hydrogen (H_2) into reactive atomic hydrogen species, which can then be adsorbed onto or diffused into the catalyst.[7] This mechanism facilitates the storage of substantial quantities of hydrogen under relatively

[a]*Institute of Chemical Sciences, Bahauddin Zakariya University, Multan, 60800, Pakistan*
[b]*Department of Physiology and Biochemistry, Cholistan University of Veterinary and Animal Sciences, Bahawalpur, 63100 Pakistan. E-mail: myar@cuvas.edu.pk*
[c]*Center for Scientific Research and Entrepreneurship, Northern Border University, Arar, 73213 Saudi Arabia*
[d]*Department of Chemistry, COMSATS University, Abbottabad Campus, KPK, 22060, Pakistan. E-mail: sehrishsarfaraz555@gmail.com*
[e]*Department of Chemistry, Faculty of Science, Islamic University of Madinah, P.O. Box 170, Madinah, 42351, Saudi Arabia. E-mail: yasser.riyad@iu.edu.sa*

mild conditions of pressure and temperature.[8] The kinetics of hydrogen dissociation in metal–hydrogen systems are strongly influenced by thermodynamic parameters, particularly temperature and pressure.[9,10] The capability of metals to dissociate hydrogen varies according to their electronic structure and surface properties.[11] Importantly, in hydrogenation reactions, the dissociation of H_2 is regarded as one of the rate-limiting steps, thus highlighting the importance of understanding the nature and behavior of active sites on catalytic surfaces.[12] This has led to extensive research into optimizing metal-based catalysts for improved dissociation performance. Furthermore, catalytic adsorption and activation of molecular hydrogen are fundamental steps in large-scale hydrogenation and dehydrogenation processes.[13] Typically, hydrogen is first physisorbed or chemisorbed onto the catalyst surface, followed by its dissociation into reactive hydrogen atoms.[14] Therefore, a detailed understanding of the elementary mechanisms involved in hydrogen dissociation is vital for the rational design of high-efficiency catalysts. One of the persistent challenges in advancing the hydrogen economy remains the development of materials capable of storing hydrogen in a safe and energy-efficient manner.

Catalysts play a pivotal role in advancing hydrogen dissociation reactions (HDRs), which are essential for hydrogen storage and energy conversion technologies. While noble metals like platinum,[15] palladium,[16] rhodium,[17] ruthenium,[18] and gold[19] demonstrate superior catalytic performance for the HDR, their limited availability and high cost hinder large-scale application. To address these limitations, research is increasingly focused on developing cost-effective alternatives that do not compromise efficiency. Single-atom catalysts (SACs) have emerged as a highly promising class of materials for the HDR due to their exceptional atom utilization and catalytic activity.[20] In SACs, individual metal atoms are uniformly anchored on suitable supports, offering highly active and accessible sites for hydrogen molecule adsorption and dissociation.[21] Although SACs show great potential in the HDR, deeper insights into their mechanistic behavior and long-term stability are still needed to optimize their practical performance.

Traditional materials such as graphene oxide,[22] activated carbon,[23] carbon nanotubes,[24] and fullerenes[25–28] have been extensively studied for hydrogen storage applications. Yet, their pristine forms often exhibit weak interactions with hydrogen molecules, limiting their storage capacities. To overcome these limitations, various modification strategies have been employed, including doping with alkali,[29–31] alkaline earth,[32–34] and transition metals,[35–42] as well as heteroatom substitution with elements like boron (B)[43–46] and nitrogen (N).[47,48]

Among the diverse materials explored, boron nitride (BN) nanostructures have garnered considerable attention due to their exceptional thermal stability, chemical inertness, and unique electronic properties.[49–51] Notably, the $B_{12}N_{12}$ nanocage, a highly symmetrical and stable structure, has emerged as a promising candidate for hydrogen storage applications. However, pristine $B_{12}N_{12}$ exhibits limited hydrogen adsorption capabilities, primarily due to its inert surface and lack of active sites. To enhance its hydrogen storage performance, recent studies have investigated the doping of $B_{12}N_{12}$ with various transition metals.[52,53] Weng *et al.* developed porous BN materials with tailored textures and chemical features to study hydrogen adsorption.[54] Co and Pt-functionalized, carbon-doped h-BN structures achieved remarkable hydrogen storage up to 24.9 wt%.[55] Hu *et al.* employed DFT to explore Si_2BN monolayers, reporting H_2 adsorption energies between 0.187 and 0.214 eV.[56] Banerjee *et al*. found that Li atoms on BN nanosheets resist clustering, supporting stable hydrogen storage.[57] Bhattacharya *et al.* showed that Ti doping in graphene, BN, and BC_4N prevents metal clustering, enhancing hydrogen uptake.[58] Chen *et al.* synthesized BN nanotubes on a large scale, while carbon-doped BN structures dispersed with Sc stored up to six H_2 molecules.[59,60] Bis-BN cyclohexane exhibited high kinetic stability and fast hydrogen release under catalytic conditions. Similarly, Rakrai *et al.* explored the hydrogen storage and sensing capabilities of group 8B transition metal-doped $B_{12}N_{12}$ nanocages. Their DFT calculations demonstrated that doping with metals like Os and Ir not only strengthens the interaction between hydrogen molecules and the nanocage but also reduces the energy gap, thereby improving the material's hydrogen adsorption capacity.[61] Ni-doped $B_{12}N_{12}$ clusters have been investigated for their hydrogen adsorption properties, revealing that the presence of Ni atoms facilitates the dissociation of hydrogen molecules and alters the electronic structure of the nanocage, thereby improving storage performance.[62]

Despite these advancements, a comprehensive understanding of the hydrogen adsorption and dissociation mechanisms of first-row transition metal-anchored $B_{12}N_{12}$ nanocages remains limited. In the present study, a novel $B_{12}N_{12}$ nanocage structure has been designed and systematically explored for hydrogen adsorption and dissociation using DFT. The proposed nanoring framework is composed of eight six-membered (hexagonal) and six four-membered (tetragonal) B–N rings. To the best of our knowledge, this specific $B_{12}N_{12}$ nanoring architecture is reported for hydrogen splitting applications for the first time. The hydrogen activation and storage capabilities of first-row transition metal (Sc–Zn) decorated $B_{12}N_{12}$ nanocages have been investigated, a study not previously addressed in the literature. Transition metal atoms are exohedrally anchored onto the nanocage surface, and the stability and efficiency of these complexes are evaluated through key computational descriptors including interaction energies, hydrogen adsorption energies, hydrogen activation barriers, Natural Bond Orbital (NBO) analysis, Electron Density Difference (EDD) mapping, Noncovalent Interaction (NCI) analysis, Quantum Theory of Atoms in Molecules (QTAIM) analysis, and electronic Density of States (DOS) profiles.

Computational methodology

All density functional theory (DFT) simulations in this study for the aqueous phase were performed using the Gaussian 09 software suite.[63] Geometry optimizations for all molecular

systems were carried out at the ωB97X-D/def2-TZVP level of theory.[64,65] The ωB97X-D functional, a range-separated hybrid functional with empirical dispersion corrections, has been widely recognized for its accuracy in describing noncovalent interactions, electronic structures, and reaction energy profiles.[66,67] This level of theory has been particularly effective in modeling the properties and reactivities of $B_{12}N_{12}$-based nanostructures, making it suitable for SAC applications.[68,69] As such, ωB97X-D was consistently employed throughout this work for optimizing molecular geometries and evaluating reaction mechanisms.

To characterize the nature of the stationary points on the potential energy surface (PES), vibrational frequency calculations were performed at the same theoretical level. Reactants and products were confirmed as local minima based on the complete absence of imaginary frequencies, while transition states were identified by the presence of a single imaginary frequency. These transition states were further validated through eigenvector analysis, ensuring that the imaginary mode corresponded to the reaction coordinate, thereby confirming the transition state nature. The solvent effect on the dissociation pathway was assessed by applying the PCM (polarizable continuum model)[70–72] with water as the solvent by using the same level of theory.

Optimized geometries and structural analyses were performed using GaussView 5.0[73] and Chemcraft,[74] while additional visualization and trajectory inspections were conducted using Visual Molecular Dynamics (VMD)[75] where applicable. These tools enabled comprehensive examination of spatial arrangements and electronic interactions within the anchored nanostructures.

To investigate catalytic behavior toward the HDR, first-row transition metals, specifically from Sc to Zn, were exohedrally anchored onto the $B_{12}N_{12}$ nanocage. Multiple adsorption sites were explored for each metal to determine the most stable binding configuration. Owing to the electronic diversity and open-shell nature of TMs, spin multiplicities significantly affect the stability and reactivity of the anchored systems. Therefore, for each metal-anchored complex, the first four lowest spin multiplicities, ranging up to the septet or octet states, were optimized to identify the ground-state configuration with the minimum Gibbs free energy.

Following spin-state optimization, the most thermodynamically favorable configurations were subjected to further analysis. Interaction energy calculations and mechanistic evaluations of the hydrogen dissociation process were conducted on these selected spin states. The interaction energy (E_{int}) between the metal atom and the $B_{12}N_{12}$ nanocage was computed using the standard supermolecular approach, expressed as:

$$\Delta E_{int} = E_{\mathbf{M@B_{12}N_{12}}} - (E_{B_{12}N_{12}} + E_M) \quad (1)$$

Here, $E_{\mathbf{M@B_{12}N_{12}}}$ refers to the total energy of the optimized metal-anchored complex, $E_{B_{12}N_{12}}$ denotes the energy of the isolated $B_{12}N_{12}$ nanocage, and E_M represents the energy of the isolated transition metal atom in its most stable spin multiplicity. This method provides a quantitative measure of the binding strength and thermodynamic stability of the metal-anchored complexes.

To evaluate the binding strength between the hydrogen molecule and the designed transition metal-anchored $B_{12}N_{12}$, the adsorption energy (ΔE_{ads}) was calculated using the following equation:

$$\Delta E_{ads}(H_2) = E_{\mathbf{H_2M@B_{12}N_{12}}} - \left(E_{\mathbf{M@B_{12}N_{12}}} + E_{H_2}\right) \quad (2)$$

In this equation, $E_{\mathbf{H_2M@B_{12}N_{12}}}$ represents the total energy of the hydrogen-adsorbed $\mathbf{M@B_{12}N_{12}}$ complex, E_{H_2} denotes the energy of an isolated hydrogen molecule, and $E_{\mathbf{M@B_{12}N_{12}}}$ corresponds to the energy of the optimized $\mathbf{M@B_{12}N_{12}}$.

In this study, the reaction energy (ΔE) and activation energy barrier (E_a) for hydrogen dissociation on $\mathbf{M@B_{12}N_{12}}$ complexes were computed using the following equations:

$$\Delta E = E_P - E_R \quad (3)$$

$$E_a = E_{TS} - E_R \quad (4)$$

where E_R, E_{TS}, and E_P represent the energies of the reactants, transition state, and products, respectively. These calculations provide insights into the thermodynamic feasibility and kinetic barriers of the HDR on the $\mathbf{M@B_{12}N_{12}}$ complexes. To further investigate the interaction between the donor (hydrogen molecule) and the acceptor (transition metal-anchored $B_{12}N_{12}$) species during the hydrogen dissociation process, EDD analysis was performed. This analysis highlights the redistribution of electron density upon adsorption, indicating the nature of the interaction between the hydrogen molecule and the catalyst surface. Additionally, NBO analysis was conducted at the ωB97X-D/def2-TZVP level to examine the orbital interactions and charge transfer between the hydrogen molecule and the transition metal sites. This analysis aids in understanding the bonding characteristics and electronic perturbations upon hydrogen adsorption. Furthermore, QTAIM analysis was performed using the Multiwfn 3.8 program[76] to evaluate the nature of interatomic interactions, providing a topological perspective on the bonding interactions within the $\mathbf{M@B_{12}N_{12}}$ complexes. Collectively, these computational analyses offer a comprehensive understanding of the reaction mechanisms, electronic interactions, and catalytic properties of the $\mathbf{M@B_{12}N_{12}}$ complexes in HDRs.

MD simulation

The GROMACS package was used to perform MD simulations for this study.[77,78] The ACPYPE tool generated topology files and force field parameters for nanocage complexes.[79,80] The LINCS algorithm[81] enforced constraints on all hydrogen atom bonds. The particle mesh Ewald method[82] handled electrostatic interactions at a 1.2 nm cutoff distance while van der Waals interactions received the same 1.2 nm cutoff distance. The Berendsen thermostat was used to control the temperature at 300 K before starting 100 ns production simulations to

assess the stability and dynamic behavior of the nanocage system.

Results and discussion

Optimized geometrical configurations and adsorption energetics

M@$B_{12}N_{12}$ catalysts were subjected to full geometric optimization to determine their most energetically favorable configurations before hydrogen adsorption. All optimizations were carried out using the hybrid DFT approach, specifically at the ωB97X-D/def2-TZVP level of theory. The pristine $B_{12}N_{12}$ nanocage exhibits a quasi-spherical structure comprising eight six-membered (hexagonal) and six four-membered (tetragonal) B–N rings, characterized by two distinct B–N bond lengths.[83,84] The bond length between two hexagonal rings (hh) is approximately 1.43 Å, while the bond length between a hexagonal and a tetragonal ring (ht) is about 1.47 Å. Our computed structural parameters are in strong agreement with the literature data,[52] thereby validating the reliability of the current computational methodology. The optimized structure of the pristine $B_{12}N_{12}$ cage is illustrated in Fig. 1.

To investigate the interaction between M and the $B_{12}N_{12}$ framework, various exohedral and endohedral anchoring configurations were explored. Specifically, the exohedral anchoring sites included adsorption on top of tetragonal and hexagonal rings (referred to as position 64), as well as atop the bond connecting two adjacent hexagonal rings (position 66).

Additionally, endohedral encapsulation of the TM atom within the cage was also considered. Among these configurations, the exohedral anchoring at position 64, where the M atom establishes direct bonding interactions with both tetragonal and hexagonal rings, was consistently found to be the most energetically stable across all **M@$B_{12}N_{12}$** complexes.

Spin-polarized DFT calculations were employed to identify the ground-state spin multiplicity for each complex. For each **M@$B_{12}N_{12}$** system, the four lowest possible spin states were analyzed to determine the most stable electronic configuration.

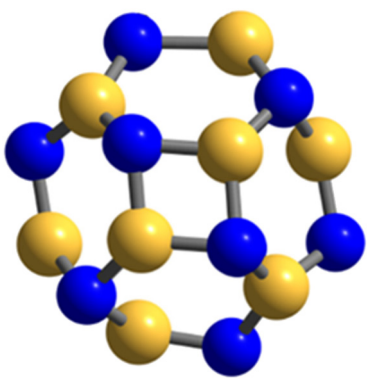

Fig. 1 Optimized molecular geometry of the isolated $B_{12}N_{12}$ nanocage. Boron atoms are depicted in yellow, while nitrogen atoms are shown in blue.

Owing to their partially filled d-orbitals, metals can exhibit a diverse range of spin states, which originate from distinct electronic arrangements including spin-up and spin-down interactions. These spin states are also significantly modulated by the nature of the metal–ligand coordination environment. The relative energies associated with the different spin states, calculated in kcal mol^{-1}, are tabulated in Table S1 (SI). These values are almost comparable to those reported in the literature.[85] The most stable spin states identified for each complex are as follows: **Sc@$B_{12}N_{12}$** (doublet), **Ti@$B_{12}N_{12}$** (triplet), **V@$B_{12}N_{12}$** (quartet), **Cr@$B_{12}N_{12}$** (quintet), **Mn@$B_{12}N_{12}$** (sextet), **Fe@$B_{12}N_{12}$** (quintet), **Co@$B_{12}N_{12}$** (quartet), **Ni@$B_{12}N_{12}$** (singlet), **Cu@$B_{12}N_{12}$** (doublet), and **Zn@$B_{12}N_{12}$** (singlet). All computations were carried out assuming neutral charge conditions for the **M@$B_{12}N_{12}$** complexes. The spin state corresponding to the lowest total electronic energy was considered the ground state and was consequently used for all subsequent analyses.

Interaction bond lengths and energies are fundamental parameters for evaluating the thermodynamic feasibility and structural integrity of molecular systems. As shown in Fig. 2, the computed distances between M atoms and the $B_{12}N_{12}$ nanocage range from 1.84 Å to 2.88 Å for M–N bonds and from 1.96 Å to 2.66 Å for M–B bonds. These values suggest that the interaction is primarily chemisorptive in nature. The **Ni@$B_{12}N_{12}$** complex demonstrates the shortest M–N and M–B bonds at 1.84 Å and 1.96 Å, respectively, which aligns with its most favorable interaction energy of −2.71 eV, indicating enhanced thermodynamic stability. In contrast, the **Zn@$B_{12}N_{12}$** system presents the longest M–N bond (2.88 Å) and M–B separation (2.66 Å).

In this study, we modeled neutral transition metals; however, the anchoring process induces noticeable charge transfer from the M atoms to the electron-deficient boron cage. This redistribution of charge endows the B–M bonds with partial ionic character, allowing them to exhibit behaviour similar to that of cationic metal centres within the otherwise neutral framework. The B–M interaction results from a mix of orbital overlap and electrostatic forces. The electron-deficient B atoms of the $B_{12}N_{12}$ cage act as suitable acceptors, engaging with the valence d-orbitals of the transition metals. As in the case of Ni, partially filled d-orbitals promote both σ-donation and π-back-donation with boron 2p orbitals, strengthening the covalent character and yielding a shorter bond length of 1.96 Å, while Zn possesses a filled d-shell that restricts effective orbital overlap, so its bonding with B is weaker and primarily electrostatic, which explains the longer separation of 2.66 Å. Overall, the differences in bond lengths across the series can be directly linked to variations in orbital interaction, charge transfer, and back-donation between the metal centers and the $B_{12}N_{12}$ framework.

Interaction energies (ΔE_{int}) for all **M@$B_{12}N_{12}$** systems were determined using the expression provided in eqn (1), and the numerical results are listed in Table 1. The consistently nega-

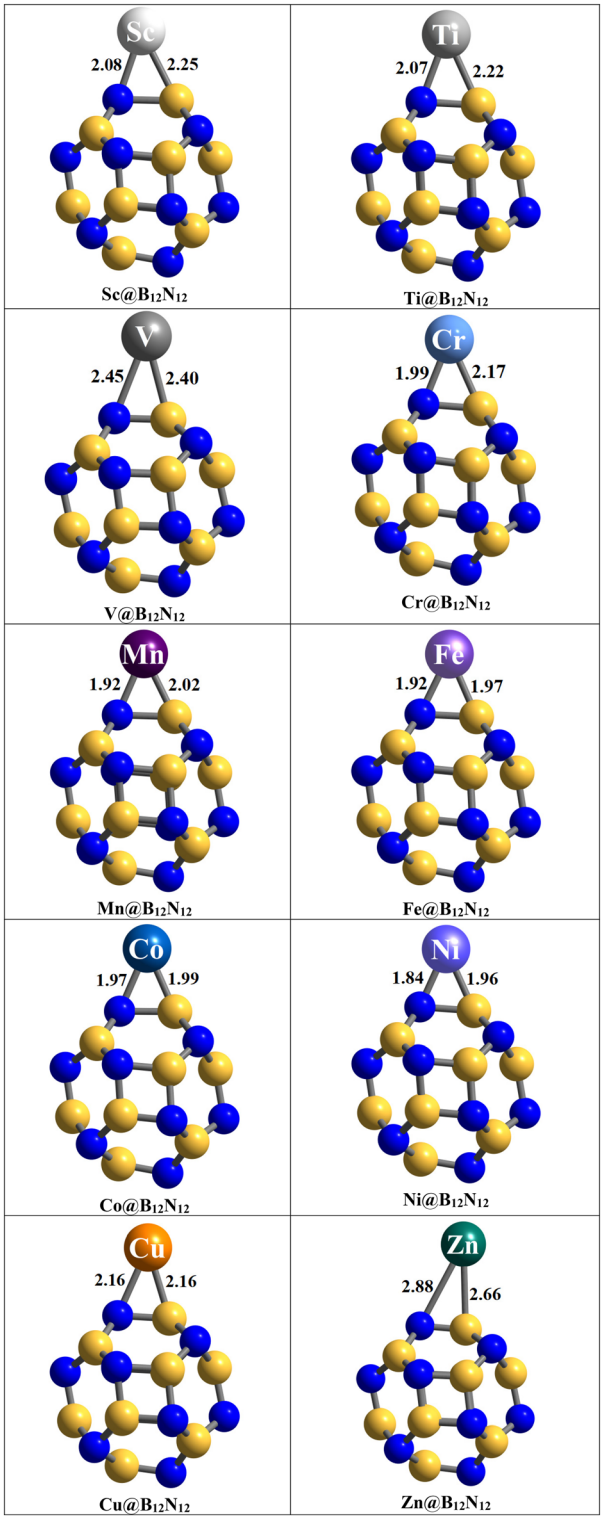

Fig. 2 Optimized molecular structures of the thermodynamically stable $M@B_{12}N_{12}$ nanocage complexes, illustrating the metal–boron (M–B) and metal–nitrogen (M–N) bond lengths.

tive values for all complexes confirm the energetic favorability of M adsorption on the $B_{12}N_{12}$ surface. Among these, **$Ni@B_{12}N_{12}$** is the most stable, exhibiting the highest interaction energy (−2.71 eV), followed by **$Cr@B_{12}N_{12}$** (−2.46 eV), both suggesting strong metal–cage interactions. This energetic stability corresponds well with the observed trend of decreasing bond lengths. The interaction energies for all systems fall within the range of −0.31 eV to −2.71 eV. Importantly, no noticeable structural deformation of the nanocage is detected after full geometry optimization, indicating the structural resilience of $B_{12}N_{12}$ upon M anchoring.

Table 1 Computed values of interaction energies (ΔE_{int}) for M adsorption on the $B_{12}N_{12}$ nanocage, hydrogen adsorption energies (ΔE_{ads}) for $H_2TM@B_{12}N_{12}$ complexes, and activation energy barriers (ΔE_a) associated with the H_2 dissociation process

Complexes	ΔE_{int} (eV)	Complexes	ΔE_{ads} (eV)	ΔE_a (eV)
$Sc@B_{12}N_{12}$	−1.01	**$H_2Sc@B_{12}N_{12}$**	−2.89	1.37
$Ti@B_{12}N_{12}$	−1.10	**$H_2Ti@B_{12}N_{12}$**	−2.96	1.20
$V@B_{12}N_{12}$	−0.31	**$H_2V@B_{12}N_{12}$**	−1.80	1.41
$Cr@B_{12}N_{12}$	−2.46	**$H_2Cr@B_{12}N_{12}$**	−2.49	0.21
$Mn@B_{12}N_{12}$	−1.17	**$H_2Mn@B_{12}N_{12}$**	−3.62	1.50
$Fe@B_{12}N_{12}$	−1.91	**$H_2Fe@B_{12}N_{12}$**	−3.38	0.19
$Co@B_{12}N_{12}$	−1.74	**$H_2Co@B_{12}N_{12}$**	−2.53	0.14
$Ni@B_{12}N_{12}$	−2.71	**$H_2Ni@B_{12}N_{12}$**	−3.61	0.16
$Cu@B_{12}N_{12}$	−0.33	**$H_2Cu@B_{12}N_{12}$**	−1.02	0.61
$Zn@B_{12}N_{12}$	−0.82	**$H_2Zn@B_{12}N_{12}$**	1.38	2.96

Hydrogen molecule adsorption on M-decorated $B_{12}N_{12}$ nanocage catalysts

Adsorption energy (E_{ads}) of an atom or molecule on a surface is quantitatively defined as the energy required to desorb the species from the surface, thereby reflecting the strength of the interaction between the adsorbate and the substrate. Typically, this process is exothermic in nature, releasing energy when a gaseous molecule binds to a surface. In the present investigation, the average E_{ads} values were calculated for hydrogen adsorption across all **$M@B_{12}N_{12}$** complexes *via* the PCM model (refer to Fig. 3). The adsorption energies for hydrogen interacting with M-decorated $B_{12}N_{12}$ nanocages are compiled in Table 1. A more negative value of E_{ads} indicates stronger and more stable binding of the hydrogen molecule to the catalyst surface, signifying an exothermic and thermodynamically favorable adsorption. In contrast, a positive E_{ads} denotes a less favorable, endothermic interaction. Accordingly, greater negativity in E_{ads} corresponds to enhanced stability of the H_2-adsorbed **$M@B_{12}N_{12}$** systems. Out of the ten **$M@B_{12}N_{12}$** complexes investigated, hydrogen adsorption was found to be energetically favorable in all systems except **$H_2Zn@B_{12}N_{12}$**, with calculated E_{ads} values ranging between −3.62 eV and −1.02 eV, implying stable hydrogen interaction without causing structural deformation. However, **$H_2Zn@B_{12}N_{12}$** exhibited positive E_{ads} values of 1.38 eV, indicating relatively weak or unfavorable adsorption. Among the catalysts studied, **$H_2Mn@B_{12}N_{12}$**, **$Ni@B_{12}N_{12}$**, and **$H_2Fe@B_{12}N_{12}$** demonstrated particularly strong hydrogen adsorption with E_{ads} values of −3.62 eV, −3.61 eV, and −3.38 eV, respectively (see Table 1 for details). The negative values of E_{ads} observed in most complexes underscore the spontaneous nature of H_2 adsorption on these M-modified

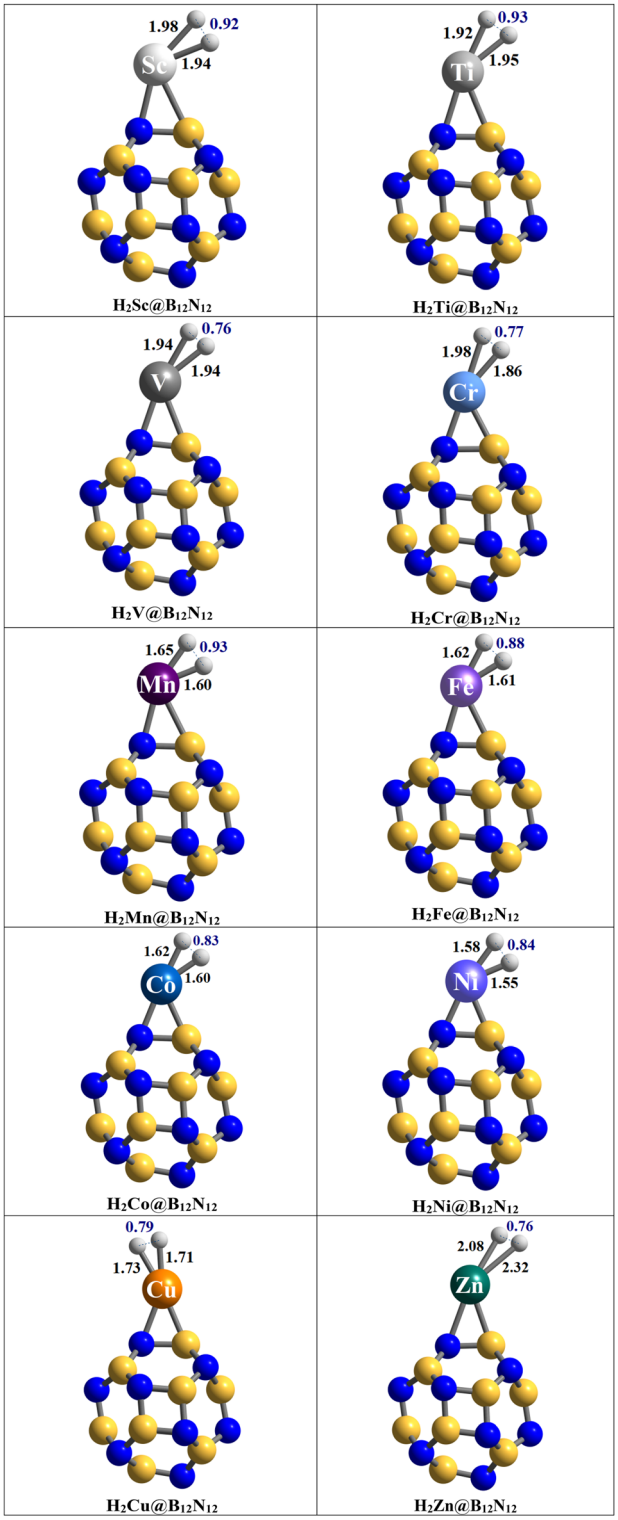

Fig. 3 Geometrically optimized configurations of hydrogen-adsorbed **M@B$_{12}$N$_{12}$** nanocage systems, highlighting key intermolecular interaction distances.

$B_{12}N_{12}$ nanocages. Structural parameters further validate the adsorption phenomena. The H–H bond length following adsorption was found to increase relative to the isolated H_2 molecule (0.74 Å), extending to values between 0.76 and 0.93 Å (see Fig. 3). This bond elongation suggests the initiation of H_2 activation on the catalyst surface. Additionally, the computed M–H interaction distances ranged from 1.55 Å to 2.23 Å, supporting the evidence of strong metal–hydrogen interactions. Among all studied systems, **H$_2$Mn@B$_{12}$N$_{12}$** exhibited the most negative E_{ads} (−3.62 eV), highlighting it as the most effective candidate for hydrogen adsorption. On the other hand, **H$_2$Zn@B$_{12}$N$_{12}$** displayed the highest positive E_{ads} (1.38 eV), implying the least favorable adsorption. Overall, the slight elongation in the H–H bond length observed across the **M@B$_{12}$N$_{12}$** systems indicates the activation of molecular hydrogen, affirming the catalytic potential of these nanostructured materials.

Hydrogen molecule dissociation on M@B$_{12}$N$_{12}$ complexes

The dissociative adsorption of molecular hydrogen (H_2) represents a fundamental step in numerous catalytic processes, particularly on M surfaces. This reaction involves the cleavage of the strong covalent H–H bond and the concurrent formation of new bonds between the resulting hydrogen atoms and the catalyst surface. Due to the energy-intensive nature of this transformation, the catalytic behavior of **M@B$_{12}$N$_{12}$** toward hydrogen dissociation has been comprehensively investigated in this study. To assess the catalytic efficiency of the **M@B$_{12}$N$_{12}$** complexes, the homolytic dissociation pathway of the adsorbed hydrogen molecule was analyzed. It involves the symmetrical splitting of H_2 into two neutral hydrogen atoms. The reaction proceeds *via* a two-step mechanism: initially, the H_2 molecule adsorbs onto the catalyst, forming an intermediate H_2* state; subsequently, the H–H bond breaks, and the resulting hydrogen atoms chemisorb on the same M center. This is evidenced by the significant elongation of the H–H bond from its equilibrium gas-phase value of ~0.74 Å to values ranging between 2.21 Å and 2.81 Å in the product state, as summarized in Table S2. Computational results indicate that the final state (2H*), where both hydrogen atoms are bound to the catalyst, is thermodynamically favored across all studied **M@B$_{12}$N$_{12}$** systems, as evidenced by consistently negative reaction energies. Fig. 4 illustrates the potential energy profiles for these dissociation processes, demonstrating that the homolytic pathway is exothermic. These findings underscore the ability of **M@B$_{12}$N$_{12}$** nanocages to act as efficient catalysts for hydrogen activation and dissociation, an essential step in various hydrogenation and energy conversion reactions.

Among the examined **M@B$_{12}$N$_{12}$** complexes for homolytic hydrogen dissociation, the **Co@B$_{12}$N$_{12}$** system exhibits the lowest activation energy, calculated at only 0.14 eV, indicating its superior catalytic efficiency for H–H bond cleavage. In contrast, **Zn@B$_{12}$N$_{12}$** presents the highest energy barrier of 2.96 eV, signifying limited catalytic performance.

The energy barriers associated with **Ni@B$_{12}$N$_{12}$** (0.16 eV), **Fe@B$_{12}$N$_{12}$** (0.19 eV), **Cr@B$_{12}$N$_{12}$** (0.21 eV), and **Cu@B$_{12}$N$_{12}$** (0.61 eV) are relatively close in magnitude, suggesting comparable activity profiles among these systems. For the remaining catalysts, the dissociation barriers are calculated

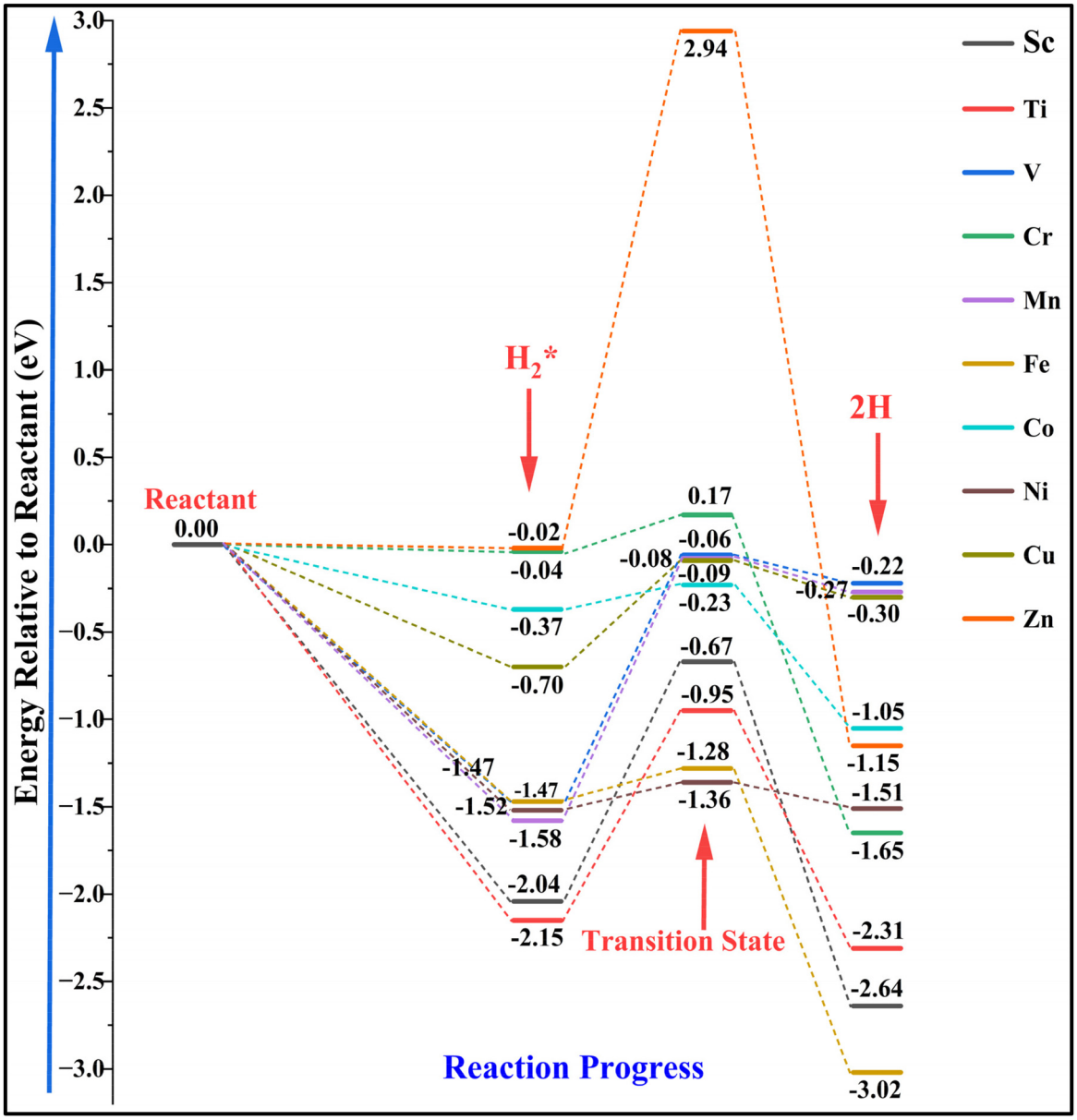

Fig. 4 Energy profiles for the HDR on **M@B$_{12}$N$_{12}$**. The relative energies of the adsorbed H_2 intermediate (H_2*), transition state, and dissociated H-atoms (2H*) to the reactant are reported in eV.

as follows: **Ti@B$_{12}$N$_{12}$** (1.20 eV), **Sc@B$_{12}$N$_{12}$** (1.37 eV), **V@B$_{12}$N$_{12}$** (1.41 eV), **Mn@B$_{12}$N$_{12}$** (1.50 eV), and **Zn@B$_{12}$N$_{12}$** (2.96 eV). Structural parameters, including selected bond lengths (in Å) and bond angles (in degrees) at key points along the reaction coordinate, namely, the intermediate, transition state, and final product configurations, are detailed in Table S2. Analysis of the H–H bond distances in the transition states reveals that all **M@B$_{12}$N$_{12}$** complexes follow an early transition state mechanism. In such cases, the transition state geometry closely resembles that of the reactant, typically requiring lower activation energy. A shorter H–H bond length in the transition state is characteristic of this early transition state behavior. The H–H bond distances in the transition state range from 1.14 to 1.35 Å, indicating bond elongation that facilitates the activation and homolytic cleavage of H_2. The ∠H–M–H bond angles are larger in the transition state compared to the intermediate, suggesting angular expansion during dissociation. Additionally, M–H bond lengths are shorter in the transition state, reflecting stronger metal–hydrogen interactions. These geometric variations are depicted in Fig. 5 and Table S2.

A noteworthy structural feature observed during the HDR process is the formation of a weak but significant interaction between the dissociated H atom and the adjacent B atom directly linked to the anchored M centre, as shown in Fig. 5. This attraction can be attributed to the enhanced Lewis acidity of the B atom, which arises from the electron-withdrawing

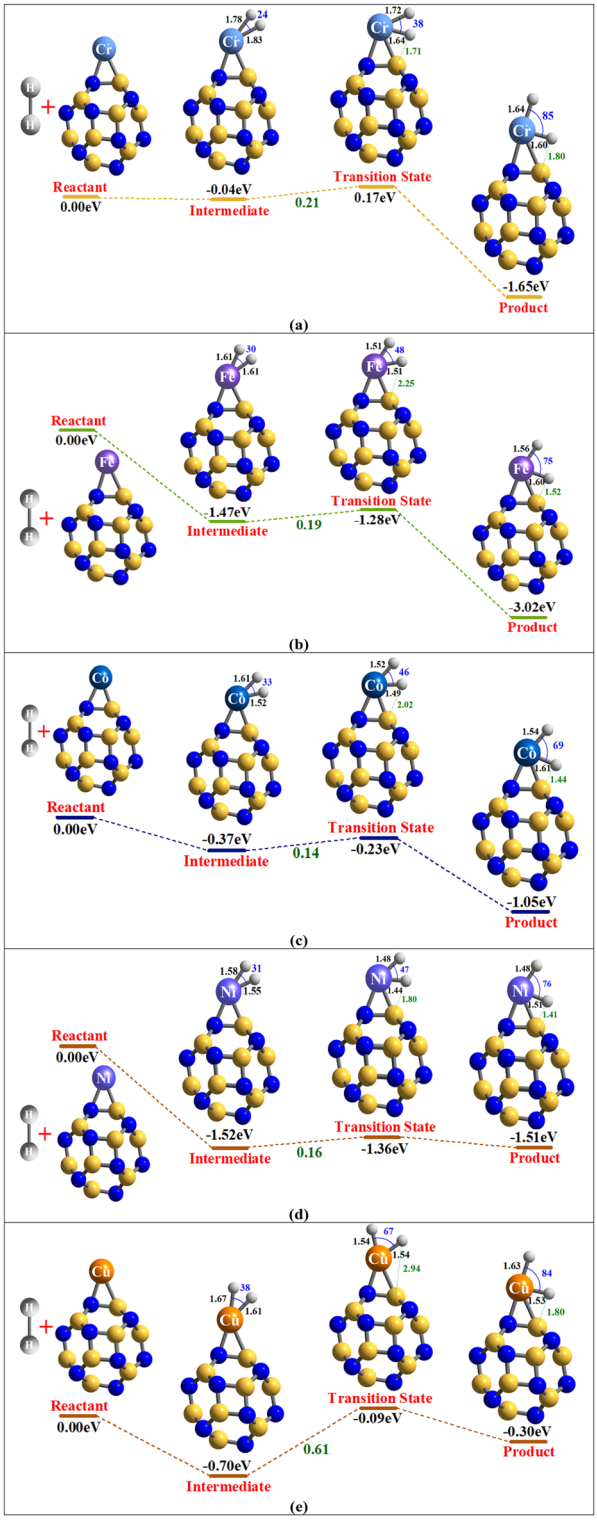

Fig. 5 Potential energy profiles illustrating the reaction pathway for hydrogen dissociation over (a) **Cr@$B_{12}N_{12}$**, (b) **Fe@$B_{12}N_{12}$**, (c) **Co@$B_{12}N_{12}$**, (d) **Ni@$B_{12}N_{12}$**, and (e) **Cu@$B_{12}N_{12}$** single-atom catalysts.

nature of the coordinated transition metal and the local electronic polarization within the cage. Such a Lewis-acidic B site can act as a secondary binding centre that stabilizes the dissociated hydrogen, effectively lowering the energy barrier for H–H bond cleavage and promoting the overall reaction kinetics. Such a secondary H–B interaction has been reported in catalytic systems involving B-doped supports and frustrated Lewis pair catalysts.[86–88] These findings highlight the dual role of the **TM@$B_{12}N_{12}$** catalyst, where both the transition metal centre and the boron framework participate synergistically in promoting hydrogen activation.

In this study, **Cr@$B_{12}N_{12}$**, **Fe@$B_{12}N_{12}$**, **Co@$B_{12}N_{12}$**, **Ni@$B_{12}N_{12}$**, and **Cu@$B_{12}N_{12}$** catalysts, identified for their superior catalytic performance, are selected as representative models for an in-depth analysis of the hydrogen dissociation process. These efficient complexes are illustrated in Fig. 5, while the energy profiles of the remaining systems are provided in the SI (Fig. S1(a)–(e)). As depicted in Fig. 5(c), the H_2 molecule initially adsorbs on the **Co@$B_{12}N_{12}$** surface, followed by homolytic cleavage into two hydrogen atoms that anchor at the Co site, overcoming a minimal activation energy barrier of 0.14 eV. Structural analysis shows the H–H bond elongates from 0.90 Å (intermediate) to 1.35 Å (transition state), accompanied by an increase in the ∠H–Co–H bond angle from 33° to 46°, indicating molecular activation. The Co–H bond lengths contract from 1.52 Å (intermediate) to 1.49 Å in the transition state. In the final product, the ∠H–Co–H bond angle expands to 69°, signifying stronger metal–hydrogen interactions and confirming bond formation. In the case of **H_2Co@$B_{12}N_{12}$**, the H–B distance decreases from 2.02 Å in the transition state to 1.44 Å in the final structure, indicating the formation of a much stronger B–H interaction that further stabilizes the dissociated hydrogen atom. The reaction releases −0.82 eV energy, and the product complex (**H_2Co@$B_{12}N_{12}$**) exhibits a lower enthalpy of −1.05 eV, indicating thermodynamic stability relative to the reactant state.

The **Ni@$B_{12}N_{12}$** complex exhibits the second lowest activation barrier for hydrogen dissociation among the studied systems. The corresponding free energy profile and structural representations are shown in Fig. 5(d). During the reaction, the H–H bond length increases from 0.93 Å in the intermediate state to 1.27 Å in the transition state, as indicated in Table S2. Concurrently, the ∠H–Ni–H bond angle widens from 31° to 47°, reflecting a shift toward product-like geometry and effective activation of the H_2 molecule. The calculated energy barrier for this process is 0.16 eV. In the transition state, Ni–H interaction distances decrease to 1.48 Å and 1.44 Å from the intermediate values of 1.58 Å and 1.55 Å. Following dissociation, the hydrogen atoms stably chemisorb at the Ni center, forming Ni–H bonds with lengths of 1.48 Å and 1.51 Å, indicating favorable bonding in the product complex and the ∠H–Ni–H bond angle further expands to 76°. The H–B separation shortens significantly from 1.80 Å in the transition state to 1.41 Å in the final configuration, pointing to the development of a stronger B–H bond that helps stabilize the dissociated hydrogen. The reaction releases −0.15 eV energy, and the product complex (**H_2Ni@$B_{12}N_{12}$**) exhibits a lower enthalpy of −1.51 eV.

For **Fe@$B_{12}N_{12}$**, the adsorbed hydrogen molecule initially possesses an H–H bond length of 0.86 Å, which undergoes

substantial elongation to 1.27 Å in the transition state, indicative of effective bond activation. The energy barrier associated with the dissociation process is computed to be 0.19 eV. In the intermediate stage, the Fe–H bond lengths are found to be 1.61 Å, which decrease to 1.51 Å, as the system transitions toward the dissociation pathway. Concurrently, the ∠H–Fe–H bond angle widens from 30° to 48°, reflecting structural reorganization and progressive cleavage of the H–H bond, as illustrated in Fig. 5(b). Post-dissociation, the two hydrogen atoms independently coordinate with the Fe center, forming stable Fe–H bonds of 1.56 Å and 1.60 Å and the ∠H–Fe–H bond angle expands to 75°. The H–B distance decreases markedly from 2.25 Å in the transition state to 1.52 Å in the final state, indicating the emergence of a stronger interaction that aids in anchoring the hydrogen atom after dissociation. Furthermore, the computed enthalpy of the product complex ($\mathbf{H_2Fe@B_{12}N_{12}}$) is −3.02 eV, confirming that the dissociated state is thermodynamically more favorable than the reactant configuration. This reaction releases −1.74 eV energy.

For the $\mathbf{Cr@B_{12}N_{12}}$ SAC, the hydrogen molecule initially exhibits a bond length of 0.85 Å upon adsorption. This bond undergoes a significant elongation to 1.24 Å in the transition state, indicating progressive activation toward dissociation. The associated activation energy for this process is calculated to be 0.21 eV. During the intermediate stage, the Cr–H bond distance is measured as 1.83 Å, which further decreases to 1.64 Å in the transition state. Concurrently, the ∠H–Cr–H bond angle increases markedly from 24° to 38°, reflecting geometric reorganization associated with H–H cleavage, as depicted in Fig. 5(a). Following dissociation, the individual hydrogen atoms establish stable interactions with the Cr center, yielding a final Cr–H bond length of 1.60 Å, and the ∠H–Cr–H bond angle expands to 85°. The H–B separation remains within the attractive range, shifting slightly from 1.71 Å in the transition state to 1.80 Å in the final state. The reaction releases −1.82 eV energy. Additionally, the computed enthalpy of the product complex ($\mathbf{H_2Cr@B_{12}N_{12}}$) is −1.65 eV, suggesting that the dissociated state is thermodynamically more stable than the initial reactant configuration.

In the case of the $\mathbf{Cu@B_{12}N_{12}}$ catalyst, the initially adsorbed H_2 molecule exhibits an H–H bond distance of 0.84 Å, which extends significantly to 1.14 Å in the transition state, indicating successful activation of the molecular hydrogen. The calculated activation energy required for the dissociation process is 0.61 eV. During the intermediate stage, the Cu–H bond lengths are observed to be 1.67 Å and 1.61 Å; these contract to 1.54 Å in the transition state. Simultaneously, the ∠H–Cu–H bond angle expands from 38° to 67°, suggesting a geometric rearrangement that facilitates bond cleavage, as shown in Fig. 5(e). Following dissociation, the hydrogen atoms anchor separately to the Cu atom, forming a robust Cu–H bond, 1.53 Å in length, and the ∠H–Cu–H bond angle expands to 84°. The H–B distance decreases notably from 2.94 Å in the transition state to 1.80 Å in the final state, indicating the emergence of a stabilizing interaction that becomes more pronounced after hydrogen dissociation. Additionally, the enthalpy of the product complex ($\mathbf{H_2Cu@B_{12}N_{12}}$) is calculated to be −0.30 eV, underscoring the thermodynamic stability of the product relative to the initial reactant complex.

As summarized in Table 1, the computed activation energy barriers for H_2 dissociation across the series of $\mathbf{M@B_{12}N_{12}}$ catalysts span a broad range, from 0.14 eV to 2.96 eV. Notably, the $\mathbf{Co@B_{12}N_{12}}$ complex exhibits the lowest energy requirement (0.14 eV) among all the transition metal-anchored $B_{12}N_{12}$ systems investigated. This minimal barrier suggests that hydrogen cleavage on the Co-functionalized nanocage can proceed efficiently under mild operational conditions, which aligns well with the fundamental prerequisites for catalytic hydrogenation processes. Therefore, the $\mathbf{Co@B_{12}N_{12}}$ system emerges as the most promising candidate for facilitating H–H bond dissociation among the series, underscoring its superior catalytic performance relative to other investigated counterparts. Here, we focused only on the adsorption and dissociation of a single H_2 molecule, since this approach captures the essential features of the catalytic mechanism at the active site. Investigating multiple H_2 adsorption events, while relevant for storage applications, is beyond the present scope and will be explored in future work.

The computed activation energy for hydrogen dissociation on the $\mathbf{Co@B_{12}N_{12}}$ complex is significantly lower than that reported for conventional noble metal-based catalysts. For instance, the dissociation barriers on Pt(111),[89] Au(111),[90] and Ag(111)[91] surfaces have been reported as 0.23 eV, 1.30 eV, and 1.55 eV, respectively. Moreover, $\mathbf{Co@B_{12}N_{12}}$ exhibits superior performance compared to various transition metal-doped nanomaterials, such as Sc@NB (0.13 eV),[92] $Zn@C_{20}$ (0.53 eV),[25] $Ni@C_2N$ (0.40 eV), and $Co@C_2N$ (0.45 eV).[93] Even in comparison with similar alloy-based systems like the $Mg_{15}Ni_2Al_{12}$ (0.53 eV) and $Mg_{17}Al_{12}$ (0.82 eV) surfaces,[94] the $\mathbf{Co@B_{12}N_{12}}$ catalyst demonstrates a markedly lower energy barrier. This comparative analysis, summarized in Table 2,

Table 2 Comparison of hydrogen dissociation barriers for various catalysts

Catalyst	Structure type	Activation barrier (eV)	Ref.
$\mathbf{Co@B_{12}N_{12}}$	SAC on nanocage	**0.14**	Present study
Pt (111)	Noble metal surface	0.23	89
Au (111)	Noble metal surface	1.30	90
Ag (111)	Noble metal surface	1.55	91
Ag (211)	Noble metal surface	1.33	91
Sc@NB	TM-doped 2D sheet	0.13	92
$Ni@C_2N$	TM-doped graphene analogue	0.40	93
$Mn@C_{24}$	TM-doped fullerene	0.04	26
$Zn@C_{20}$	TM-doped fullerene	0.53	25
$Mg_{15}Ni_2Al_{12}$	Alloy surface	0.53	94
$Ni@Mg_{17}Al_{12}$	Alloy surface	0.82	94
Mg_9Rh cluster	Cluster	0.63	95
$Sc@C_{60}$	TM-doped fullerene	0.13	28
Mg (0001)	Metal surface	1.18	96
Cu (001)	Metal surface	0.59	97

underscores the exceptional catalytic proficiency of **Co@$B_{12}N_{12}$** as a SAC for hydrogen dissociation. Owing to its minimal activation barrier, **Co@$B_{12}N_{12}$** stands out as a highly promising SAC for the efficient facilitation of the HDR.

Topological analysis of electron density using quantum theory of atoms in molecules (QTAIM)

QTAIM was employed to investigate the interatomic interactions between the hydrogen molecule and the **M@$B_{12}N_{12}$** catalytic systems. The topological parameters derived from the QTAIM analysis provide comprehensive insights into the nature of these interactions at the bond critical points (BCPs). These parameters include electron density (ρ), Laplacian of electron density ($\nabla^2\rho$), kinetic energy density (G_r), potential energy density (V_r), and total energy density (H_r). The electron density at the BCP helps assess bond strength, while the Laplacian of electron density ($\nabla^2\rho$) characterizes the interaction type. Moreover, the $-V/G$ ratio is used to evaluate the strength and nature of the interactions: a ratio greater than 2 indicates covalent bonding, while a value less than 1 corresponds to weaker interactions. The values for these parameters derived from the QTAIM analysis are provided in Table 3, and the corresponding molecular plots for the hydrogen-adsorbed **M@$B_{12}N_{12}$** complexes are shown in Fig. 6.

For all the designed catalytic systems, two metal–hydrogen BCPs were observed for each complex, as summarized in Table 3. In these **H_2M@$B_{12}N_{12}$**, two metal–hydrogen BCPs are present. The hydrogen molecule dissociates effectively upon adsorption, with both hydrogen atoms exhibiting a strong interaction. Consequently, this hydrogen dissociates over the catalyst, indicating that **H_2M@$B_{12}N_{12}$** effectively facilitates the dissociation of the hydrogen molecule. This property is crucial for the catalyst's ability to enhance catalytic performance, particularly for processes that rely on hydrogen dissociation.

Table 3 Results of the topological parameters derived from the QTAIM analysis of hydrogen-adsorbed **M@$B_{12}N_{12}$** complexes

Analyte–H_2	ρ (a.u)	$\nabla^2\rho$ (a.u)	$G(r)$ (a.u)	$V(r)$ (a.u)	$H(r)$ (a.u)	$-V/G$
Sc–H1	0.213	−0.005	0.166	−0.333	−0.167	2.01
Sc–H2	0.205	0.082	0.178	−0.336	−0.158	1.88
Ti–H1	0.047	0.123	0.036	−0.041	−0.005	1.15
Ti–H2	0.079	0.038	0.035	−0.060	−0.025	1.72
V–H1	0.153	0.342	0.187	−0.288	−0.101	1.54
V–H2	0.185	0.278	0.249	−0.429	−0.180	1.72
Cr–H1	0.054	0.186	0.051	−0.056	−0.005	1.09
Cr–H2	0.103	0.003	0.048	−0.094	−0.047	1.98
Mn–H1	0.075	0.237	0.078	−0.096	−0.018	1.24
Mn–H2	0.108	0.101	0.076	−0.127	−0.051	1.67
Fe–H1	0.097	0.391	0.127	−0.157	−0.029	1.23
Fe–H2	0.106	0.151	0.087	−0.136	−0.049	1.56
Co–H1	0.189	0.011	0.150	−0.297	−0.147	1.98
Co–H2	0.183	0.137	0.175	−0.315	−0.140	1.80
Ni–H1	0.182	0.024	0.147	−0.288	−0.141	1.96
Ni–H2	0.179	0.115	0.167	−0.304	−0.138	1.83
Cu–H1	0.175	0.048	0.151	−0.289	−0.13	1.92
Cu–H2	0.173	0.132	0.17	−0.307	−0.137	1.81
Zn–H1	0.169	0.178	0.167	−0.290	−0.123	1.74
Zn–H2	0.166	0.308	0.197	−0.318	−0.121	1.61

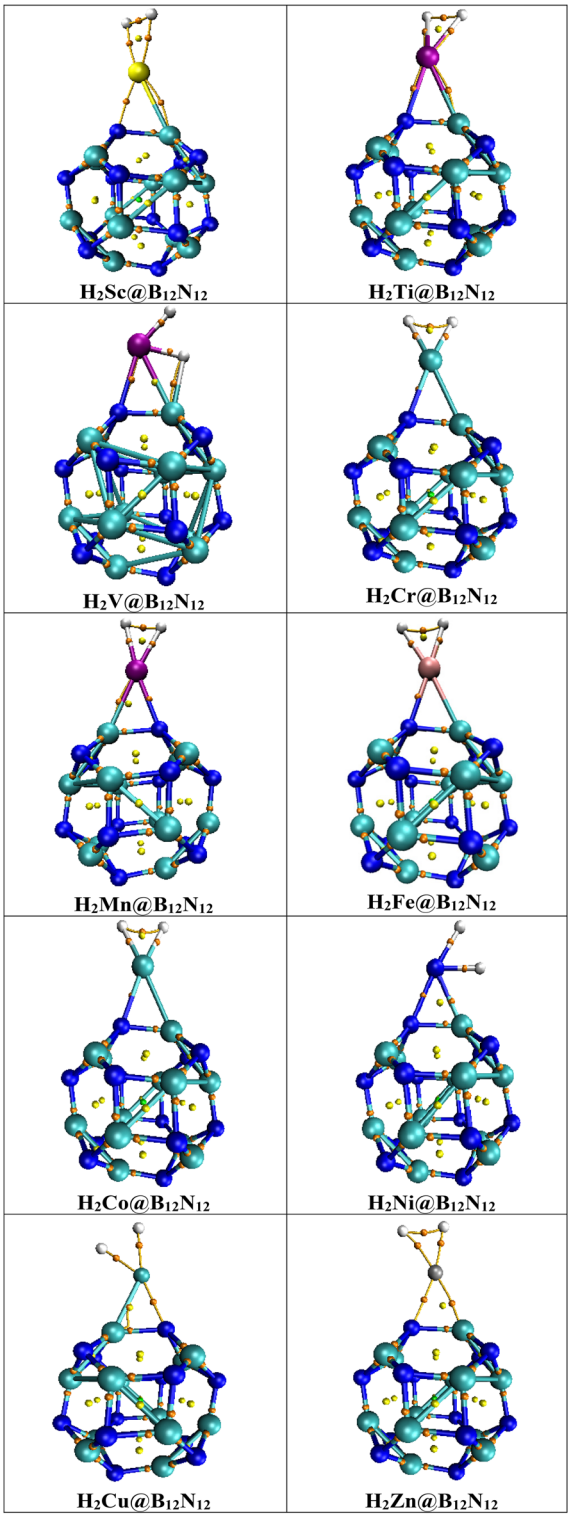

Fig. 6 Molecular plots obtained from QTAIM analysis for the hydrogen-adsorbed **M@$B_{12}N_{12}$** complexes.

The Laplacian of electron density ($\nabla^2\rho$) for the BCPs of the hydrogen-adsorbed **M@$B_{12}N_{12}$** systems ranges from −0.005 to 0.391. A value of $\nabla^2\rho$ greater than zero suggests the presence of closed-shell interactions, which are typically weaker in nature.

The H_r, which is the sum of G_r and V_r, is found to be negative for all the designed systems, confirming the presence of covalent interactions. A negative H_r value is indicative of covalent bonding, implying that the interactions between the hydrogen molecule and the catalyst are of a covalent nature.

Additionally, the $-V/G$ ratio ranges from 1.09 to 2.01, further supporting the conclusion that these interactions are covalent. Specifically, the ratios fall within the range that suggests the presence of shared electron density between the hydrogen molecule and the metal centers, thus reinforcing the covalent or shared-shell nature of the interactions.

These QTAIM-derived results provide an in-depth understanding of the interatomic interactions, offering insights that cannot be directly obtained through structural analysis alone. Moreover, the findings are consistent with the computed adsorption energies and reactivity profiles of the complexes, providing further validation of the QTAIM analysis. This consistency demonstrates that the QTAIM results accurately reflect the bonding characteristics and catalytic behavior of the systems. In particular, the ability of **Co@$B_{12}N_{12}$** to support the dissociation of hydrogen after adsorption highlights its role in promoting efficient catalytic processes, thereby enhancing the overall catalytic performance of the system. This reaffirms the significance of QTAIM in characterizing the bonding interactions and their implications for catalytic activity.

Analysis of the electronic structure *via* natural bond orbitals and electron density difference mapping

EDD and NBO analyses were performed to unravel the mechanism of H_2 activation and dissociation on the **M@$B_{12}N_{12}$** catalysts. NBO calculations (Table 4) quantify electron transfer from the metal 3d orbitals to the adsorbed H_2 molecule: in every H_2* + **M@$B_{12}N_{12}$** complex, the transition-metal center acquires a net positive charge, evidence of its electron-donor role driven by its electropositive character; while both hydrogen atoms bear negative charges in **H_2Sc@$B_{12}N_{12}$**, only one hydrogen bears a negative charge in **H_2Cr@$B_{12}N_{12}$**, **H_2Mn@$B_{12}N_{12}$**, and **H_2Zn@$B_{12}N_{12}$**. In all other systems, both hydrogens display a slightly positive value. Among the series, scandium donates the most charge (+1.037*e*), and nickel the least (+0.329*e*).

Table 4 Natural bond orbital-derived charge allocations for the H_2-adsorbed **M@$B_{12}N_{12}$** complexes

Complexes	H1 (e)	M (e)	H2 (e)
H_2Sc@$B_{12}N_{12}$	−0.021	1.037	−0.003
H_2Ti@$B_{12}N_{12}$	0.027	0.869	0.012
H_2V@$B_{12}N_{12}$	0.014	0.506	0.014
H_2Cr@$B_{12}N_{12}$	0.061	0.695	−0.008
H_2Mn@$B_{12}N_{12}$	0.056	0.516	−0.026
H_2Fe@$B_{12}N_{12}$	0.069	0.357	0.033
H_2Co@$B_{12}N_{12}$	0.072	0.341	0.030
H_2Ni@$B_{12}N_{12}$	0.035	0.329	0.016
H_2Cu@$B_{12}N_{12}$	0.025	0.527	0.040
H_2Zn@$B_{12}N_{12}$	−0.037	0.702	0.034

Focusing on the representative **Co@$B_{12}N_{12}$** system, adsorption induces +0.341*e* charge at Co, with H1 and H2 carrying +0.072*e* and +0.030*e*, respectively. EDD maps corroborate this directional charge flow by showing depletion around Co and accumulation at the hydrogen sites, as displayed in Fig. 7. The injected electrons populate the H_2 σ* antibonding orbital, weakening and elongating the H–H bond until cleavage occurs. Together, the NBO and EDD results confirm that metal-to-hydrogen electron transfer into antibonding orbitals is the key driver of efficient H_2 splitting on **M@$B_{12}N_{12}$**, underscoring the strong metal–hydrogen binding that enables self-dissociation of the molecule.

EDD analysis was performed to validate the NBO-derived charge transfer upon H_2 adsorption. The EDD isosurfaces for all hydrogen-adsorbed **M@$B_{12}N_{12}$** complexes are displayed in Fig. 7, where purple-blue regions denote electron depletion and red-orange regions indicate electron accumulation. In all systems, purple-blue isosurfaces are predominantly localized on the transition-metal center and hydrogen atoms, signifying regions of electron-density depletion. These maps clearly show electron donation from the transition-metal centers to both H1 and H2 upon adsorption, in excellent agreement with the NBO results. This transferred electron density populates the σ* antibonding orbital of the hydrogen molecule, weakening the H–H bond and thereby facilitating its dissociation over the **M@$B_{12}N_{12}$** catalysts.

Collectively, our QTAIM, NBO, and EDD findings establish that transition-metal-anchored $B_{12}N_{12}$ nanocages serve as highly effective single-atom catalysts for the HDR. In particular, **Co@$B_{12}N_{12}$** exhibits an exceptionally low activation barrier of 0.14 eV, underscoring its promise as a high-performance electrocatalyst. These insights pave the way for the rational design of heteroatom-anchored nanocage SACs tailored to promote facile hydrogen splitting.

Reduced density gradient (RDG) analysis

Reduced density gradient (RDG) analysis was conducted using Multiwfn 3.8[76] to map regions of low electron-density variation and thus identify any noncovalent (closed-shell) interactions within the **H_2M@$B_{12}N_{12}$** complexes. In this approach, the reduced density gradient is plotted against $\mathrm{sign}(\lambda_2)\rho$, where λ_2 is the second eigenvalue of the electron-density Hessian and ρ is the electron density enabling discrimination between attractive and repulsive contacts. Conventionally, spikes in the 2D RDG *vs.* $\mathrm{sign}(\lambda_2)\rho$ plot near $\mathrm{sign}(\lambda_2)\rho \approx 0$ ($\rho > 0$) reflect weak van der Waals interactions, whereas negative $\mathrm{sign}(\lambda_2)\rho$ values (below −0.02 a.u.) are characteristic of strong attractive (covalent-like) interactions.[98] As shown in Fig. 8, none of the **H_2M@$B_{12}N_{12}$** complexes exhibit the hallmark peaks around $\mathrm{sign}(\lambda_2)\rho \approx 0$, confirming the absence of significant hydrogen bond or dispersion contacts. Three-dimensional RDG isosurfaces rendered in VMD[75] further substantiate this finding: greenish regions, which would indicate weak noncovalent interactions, are absent, while only blue-tinged lobes appear between the TM centers and the hydrogen atoms, signaling strong, attractive (shared-shell) bonding. Red cylindrical pro-

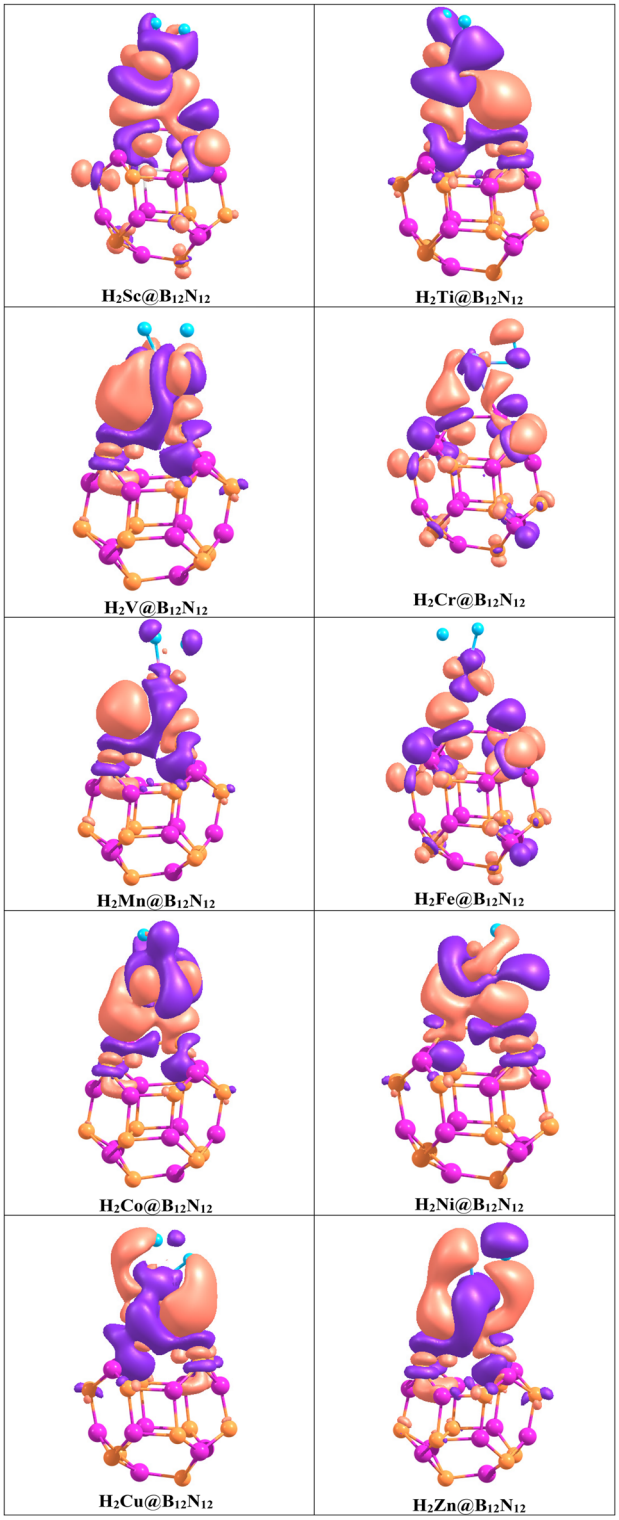

Fig. 7 Electron density difference isosurfaces for hydrogen-adsorbed **M@B$_{12}$N$_{12}$** complexes. Red-orange: electron accumulation; purple-blue: electron depletion.

jections highlight zones of positive $\lambda_2\rho$, corresponding to steric repulsion that may contribute to homolytic H–H bond elongation. These observations confirm that H–M bonding in all **H$_2$M@B$_{12}$N$_{12}$** catalysts is dominated by covalent interactions, in agreement with their comparable electronegativities and previous studies on metal-doped $B_{12}N_{12}$ surfaces[99–101] for hydrogen dissociation. By ruling out competing noncovalent forces, RDG analysis underscores the intrinsic ability of these SACs to facilitate efficient H_2 cleavage *via* strong orbital overlap and electron-density redistribution.

Electronic properties of molecular hydrogen adsorbed M@B$_{12}$N$_{12}$

To elucidate the electronic interactions between hydrogen molecules and the **M@B$_{12}$N$_{12}$** catalysts, Density of States (DOS) and Frontier Molecular Orbital (FMO) analyses were conducted following hydrogen adsorption. The calculated energies of the HOMO and the LUMO, along with the corresponding energy gaps (E_{gap}), are compiled in Table 5. These values provide insights into the electronic properties and potential reactivity of the catalysts. The interaction between the adsorbed H_2 and the **M@B$_{12}$N$_{12}$** nanocages was further examined through TDOS and PDOS spectra. Fig. S2 illustrates the TDOS and PDOS spectra of **M@B$_{12}$N$_{12}$** complexes before the adsorption of hydrogen. Fig. S3 illustrates the TDOS and PDOS spectra for the hydrogen-adsorbed **M@B$_{12}$N$_{12}$** complexes. The changes can be clearly observed by comparing Fig. S2 and S3. Among the studied complexes, the **Co@B$_{12}$N$_{12}$** complex exhibits the most significant increase in the HOMO–LUMO gap upon hydrogen adsorption, increasing by 0.80 eV (from 7.71 to 8.51 eV), which suggests a significant stabilization of the electronic structure and improved chemical hardness after H_2 activation. Conversely, a reduction in the energy gap is observed for the **Sc@B$_{12}$N$_{12}$**, **Fe@B$_{12}$N$_{12}$**, **Cu@B$_{12}$N$_{12}$**, and **Zn@B$_{12}$N$_{12}$** complexes. This reduction is corroborated by the appearance of new peaks in their DOS spectra post hydrogen adsorption. For the remaining complexes such as **Ti@B$_{12}$N$_{12}$**, **V@B$_{12}$N$_{12}$**, **Cr@B$_{12}$N$_{12}$**, **Mn@B$_{12}$N$_{12}$**, and **Ni@B$_{12}$N$_{12}$**, an increase in the energy gap is noted. Specifically, the **H$_2$Co@B$_{12}$N$_{12}$** complex exhibits an energy gap of 8.51 eV, **H$_2$Mn@B$_{12}$N$_{12}$** shows 7.88 eV, **H$_2$Fe@B$_{12}$N$_{12}$** has 7.02 eV, **H$_2$Ni@B$_{12}$N$_{12}$** presents 7.65 eV, and **H$_2$Cu@B$_{12}$N$_{12}$** demonstrates 5.90 eV. These findings suggest enhanced hydrogen dissociation reaction (HDR) activity for these catalysts. The designed SACs anchored on the $B_{12}N_{12}$ nanocage exhibit superior catalytic performance for the HDR compared to other noble metal-based and metal-doped clusters. Notably, the **Co@B$_{12}$N$_{12}$** complex emerges as a promising SAC, effectively catalyzing the HDR process.

Molecular dynamics simulation

Root mean square deviation (RMSD). The RMSD plot shown in Fig. 9 illustrates the structural behavior of the **Co@B$_{12}$N$_{12}$** nanocage during a 100 ns molecular dynamics simulation. Throughout the simulation, the system retained a highly stable configuration, with RMSD values confined within a narrow range of 0.03–0.09 Å and an average value of approximately 0.06 Å. The absence of significant drifts or abrupt fluctuations reflects the robustness of the nanocage framework. The Co atom remained securely positioned within the $B_{12}N_{12}$ cavity for the entire simulation period, indicating strong structural confine-

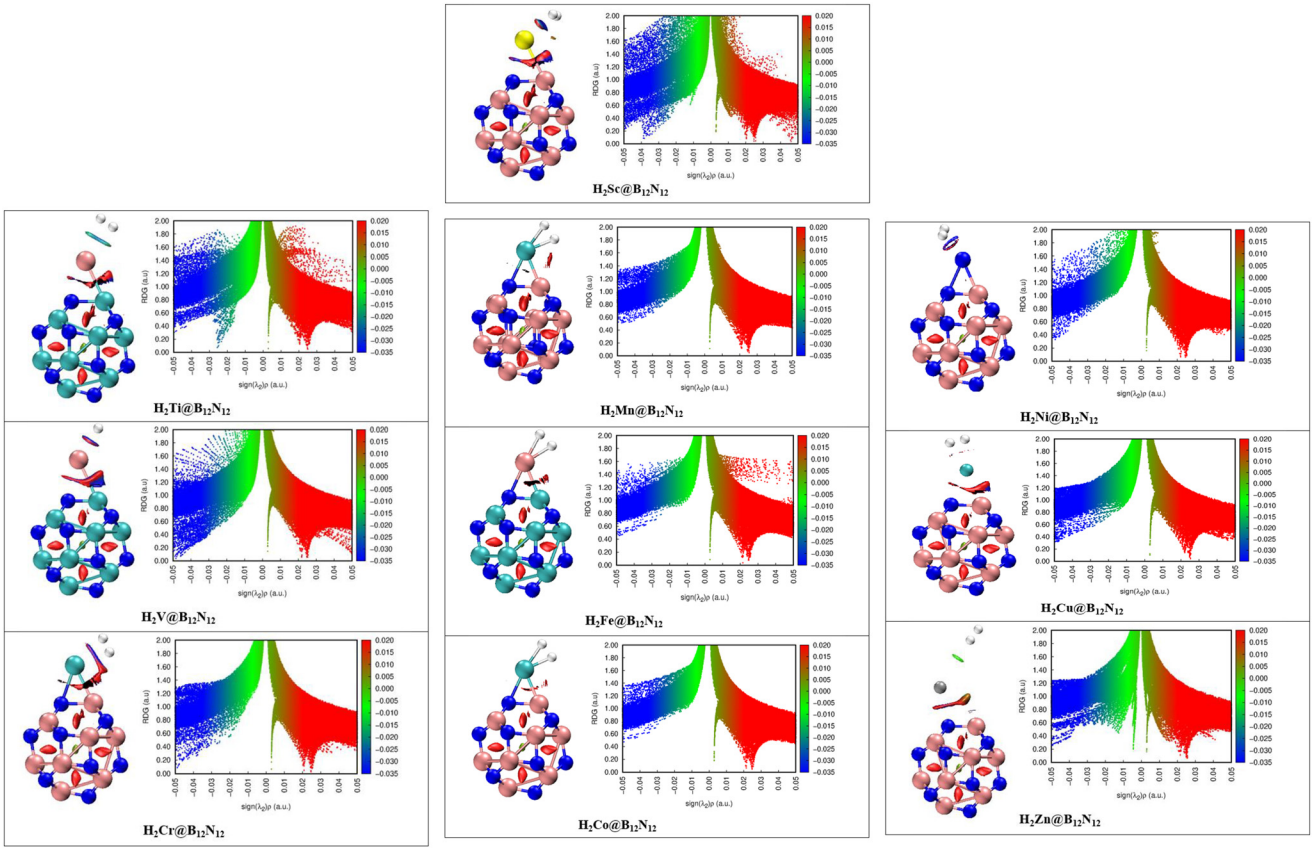

Fig. 8 Reduced density gradient (RDG) analysis of representative **M@B$_{12}$N$_{12}$** complexes, featuring three-dimensional RDG isosurfaces to visualize interaction regions and the corresponding two-dimensional RDG *versus* sign(λ_2)ρ spectra.

Table 5 Outcome of the calculated energies of the HOMO and LUMO, as well as the associated HOMO–LUMO energy gaps (ΔE_{gap}), for **M@B$_{12}$N$_{12}$** and **H$_2$M@B$_{12}$N$_{12}$** complexes (expressed in eV)

M@B$_{12}$N$_{12}$	HOMO	LUMO	E_{gap} (ΔE)
Sc@B$_{12}$N$_{12}$	−6.43	−0.36	6.07
H$_2$Sc@B$_{12}$N$_{12}$	−6.87	−1.00	5.87
Ti@B$_{12}$N$_{12}$	−6.73	−0.53	6.20
H$_2$Ti@B$_{12}$N$_{12}$	−7.26	−0.83	6.43
V@B$_{12}$N$_{12}$	−6.13	−0.06	6.07
H$_2$V@B$_{12}$N$_{12}$	−6.66	−0.14	6.53
Cr@B$_{12}$N$_{12}$	−7.78	−0.79	6.99
H$_2$Cr@B$_{12}$N$_{12}$	−8.26	−0.71	7.55
Mn@B$_{12}$N$_{12}$	−8.59	−0.80	7.78
H$_2$Mn@B$_{12}$N$_{12}$	−8.67	−0.80	7.88
Fe@B$_{12}$N$_{12}$	−7.74	−0.53	7.21
H$_2$Fe@B$_{12}$N$_{12}$	−7.93	−0.91	7.02
Co@B$_{12}$N$_{12}$	−7.93	−0.22	7.71
H$_2$Co@B$_{12}$N$_{12}$	−8.93	−0.42	8.51
Ni@B$_{12}$N$_{12}$	−7.91	−0.33	7.58
H$_2$Ni@B$_{12}$N$_{12}$	−8.18	−0.54	7.65
Cu@B$_{12}$N$_{12}$	−6.67	−0.15	6.52
H$_2$Cu@B$_{12}$N$_{12}$	−6.93	−1.03	5.90
Zn@B$_{12}$N$_{12}$	−8.51	−0.37	8.14
H$_2$Zn@B$_{12}$N$_{12}$	−6.17	−0.19	5.98

ment. The minor variations observed in RMSD values are consistent with normal atomic motions that occur under equilibrium conditions. Overall, the simulation confirms that the

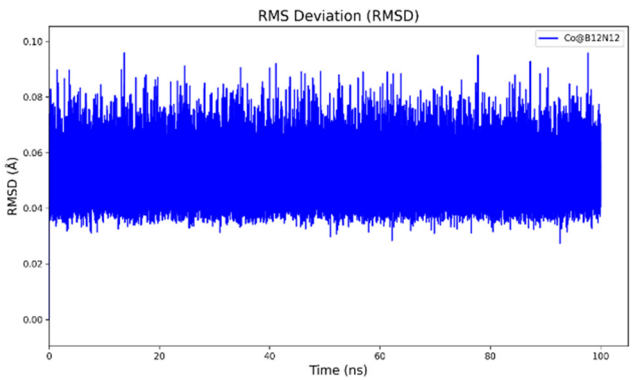

Fig. 9 RMSD of **Co@B$_{12}$N$_{12}$** during MD simulation of 100 ns.

Co@B$_{12}$N$_{12}$ nanocage preserved its integrity and structural consistency throughout the 100 ns trajectory, verifying its dynamic and thermal stability under the applied simulation parameters.

Conclusion

This DFT-based study presents an in-depth analysis of first-row transition metal-anchored $B_{12}N_{12}$ nanoclusters (**M@B$_{12}$N$_{12}$**) as SACs for hydrogen dissociation. The anchoring

of metals onto the $B_{12}N_{12}$ framework is thermodynamically favorable, with **Ni@$B_{12}N_{12}$** showing the strongest metal–support interaction. Hydrogen adsorption and dissociation studies reveal that the formation of two adsorbed hydrogen atoms (2H*) is energetically preferred, indicating an exothermic reaction profile. Notably, **Co@$B_{12}N_{12}$** demonstrates the lowest activation barrier (0.14 eV), confirming its superior catalytic performance for H–H bond cleavage. Electronic structure analyses, NBO and EDD, highlight efficient charge transfer from the metal to the H_2 molecule, leading to σ* orbital population and bond weakening. QTAIM and NCI analyses confirm covalent (shared-shell) interactions, while RDG plots further emphasize the role of short-range covalent forces in promoting the HDR. In summary, **Co@$B_{12}N_{12}$** emerges as a highly promising, noble metal-free electrocatalyst. These insights not only deepen our understanding of the SAC-mediated HDR but also guide the rational design of advanced catalysts for hydrogen-related energy applications.

Author contributions

Zainab Fareed: data curation, writing – original draft, writing – review & editing, software and data analysis. Tayyaba Tariq: data curation. Shaaban M. Shaaban: writing – review & editing. Muhammad Yar: project administration, software, and supervision. Muhammad Ali Khan: project administration, resources, supervision, writing – review & editing. Ajaz Hussain: conceptualization. Khurhsid Ayub: writing – review & editing. Sehrish Sarfaraz: software and data analysis. Yasser M. Riyad: funding acquisition.

Conflicts of interest

There are no conflicts to declare.

Data availability

The data supporting this article have been included as part of the supplementary information (SI). The supplementary information includes energies of spin-polarized complexes along with spin-states, Key bond lengths (in Å) and bond angles (in degrees) for the intermediate, transition state, and product structures of $H_2M@B_{12}N_{12}$ nanocage complexes, potential energy profiles illustrating the reaction pathway for hydrogen dissociation over (a) $Sc@B_{12}N_{12}$, (b) $Ti@B_{12}N_{12}$, (c) $V@B_{12}N_{12}$, (d) $Mn@B_{12}N_{12}$, and (e) $Zn@B_{12}N_{12}$ single-atom catalysts and DOS profile of all $H_2M@B_{12}N_{12}$ complexes after the adsorption of Hydrogen. See DOI: https://doi.org/10.1039/d5dt01548k.

Acknowledgements

The researchers wish to extend their sincere gratitude to the Deanship of Scientific Research at the Islamic University of Madinah for the support provided to the Post-Publishing Program.

References

1 J. Wang and W. Azam, *Geosci. Front.*, 2024, **15**, 101757.
2 M. Filonchyk, M. P. Peterson, L. Zhang, V. Hurynovich and Y. He, *Sci. Total Environ.*, 2024, 173359.
3 T. T. Le, P. Sharma, B. J. Bora, V. D. Tran, T. H. Truong, H. C. Le and P. Q. P. Nguyen, *Int. J. Hydrogen Energy*, 2024, **54**, 791–816.
4 Q. Hassan, S. Algburi, A. Z. Sameen, H. M. Salman and A. K. Al-Jiboory, *Energy Harvesting Syst.*, 2024, **11**, 20220127.
5 S. A. Alavi-Borazjani, S. Adeel and V. Chkoniya, *Energies*, 2025, **18**, 1231.
6 S. Evro, B. A. Oni and O. S. Tomomewo, *Int. J. Hydrogen Energy*, 2024, **78**, 1449–1467.
7 N. Dimitratos, G. Vilé, S. Albonetti, F. Cavani, J. Fiorio, N. López, L. M. Rossi and R. Wojcieszak, *Nat. Rev. Chem.*, 2024, **8**, 195–210.
8 S. Bosu and N. Rajamohan, *Int. J. Hydrogen Energy*, 2024, **52**, 352–370.
9 M. V. Lototskyy, V. A. Yartys, B. P. Tarasov, M. W. Davids, R. V. Denys and S. Tai, *Int. J. Hydrogen Energy*, 2021, **46**, 2330–2338.
10 M. Li, W. Yin, J. Pan, Y. Zhu, N. Sun, X. Zhang, Y. Wan, Z. Luo, L. Yi and L. Wang, *Chem. Eng. J.*, 2023, **471**, 144691.
11 A. D. Zolotarenko, A. D. Zolotarenko, A. Veziroglu, T. Veziroglu, N. Shvachko, A. Pomytkin, D. Schur, N. Gavrylyuk, T. Ramazanov and N. Akhanova, *Int. J. Hydrogen Energy*, 2022, **47**, 7310–7327.
12 F. Sun, Q. Tang and D.-E. Jiang, *ACS Catal.*, 2022, **12**, 8404–8433.
13 E. Rakić, M. Grilc and B. Likozar, *Chem. Eng. J.*, 2023, **472**, 144836.
14 D. R. Aireddy and K. Ding, *ACS Catal.*, 2022, **12**, 4707–4723.
15 B. Qiao, A. Wang, X. Yang, L. F. Allard, Z. Jiang, Y. Cui, J. Liu, J. Li and T. Zhang, *Nat. Chem.*, 2011, **3**, 634–641.
16 B. D. Adams and A. Chen, *Mater. Today*, 2011, **14**, 282–289.
17 T. K. Ghosh and N. N. Nair, *ChemCatChem*, 2013, **5**, 1811–1821.
18 M. Xiao, L. Gao, Y. Wang, X. Wang, J. Zhu, Z. Jin, C. Liu, H. Chen, G. Li and J. Ge, *J. Am. Chem. Soc.*, 2019, **141**, 19800–19806.
19 X. Liu, Y. Yang, M. Chu, T. Duan, C. Meng and Y. Han, *Catal. Sci. Technol.*, 2016, **6**, 1632–1641.
20 W. Guo, Z. Wang, X. Wang and Y. Wu, *Adv. Mater.*, 2021, **33**, 2004287.
21 C. Zhang, H. Wang, H. Yu, K. Yi, W. Zhang, X. Yuan, J. Huang, Y. Deng and G. Zeng, *Adv. Energy Mater.*, 2022, **12**, 2200875.

22 L. Wang, K. Lee, Y.-Y. Sun, M. Lucking, Z. Chen, J. J. Zhao and S. B. Zhang, *ACS Nano*, 2009, **3**, 2995–3000.
23 N. M. Musyoka, M. Wdowin, K. M. Rambau, W. Franus, R. Panek, J. Madej and D. Czarna-Juszkiewicz, *Renewable Energy*, 2020, **155**, 1264–1271.
24 S. Pinjari, T. Bera, G. Kapur and E. Kjeang, *Int. J. Hydrogen Energy*, 2023, **48**, 1930–1942.
25 S. Sarfaraz, M. Yar, N. S. Sheikh, I. Bayach and K. Ayub, *ACS Omega*, 2023, **8**, 14077–14088.
26 S. Sarfaraz, M. Yar, R. Hussain and K. Ayub, *Int. J. Hydrogen Energy*, 2023, **48**, 20633–20645.
27 E. Germán, J. A. Alonso, E. Janssens and M. J. López, *Int. J. Hydrogen Energy*, 2021, **46**, 20594–20606.
28 S. Sarfaraz, M. Yar, A. Hussain, A. Lakhani, A. Gulzar, M. Ans, U. Rashid, M. Hussain, S. Muhammad and I. Bayach, *ACS Omega*, 2023, **8**, 36493–36505.
29 R. Haddon, *Acc. Chem. Res.*, 1992, **25**, 127–133.
30 A. Omidvar and A. Mohajeri, *Int. J. Hydrogen Energy*, 2017, **42**, 12327–12338.
31 R. Murugavel, A. A. Rownaghi and F. Rezaei, *Energy Fuels*, 2023, **37**, 19292–19303.
32 F. Lopez-Urias, M. Terrones and H. Terrones, *Carbon*, 2015, **84**, 317–326.
33 O. Olaniyan, *Ab initio study of the beryllium-sulphur and beryllium-nitrogen co-doped graphene for nanoelectronic and optoelectronic devices*, University of Pretoria, South Africa, 2018.
34 S. Ghosh and V. Padmanabhan, *Int. J. Hydrogen Energy*, 2017, **42**, 24237–24246.
35 R. J. Toh, H. L. Poh, Z. Sofer and M. Pumera, *Chem. – Asian J.*, 2013, **8**, 1295–1300.
36 H. Lee and J. A. Hong, *Nanoscale Res. Lett.*, 2017, **12**, 426.
37 N. Ya'aini, A. Pillay, L. G. Krishnan and A. Ripin, *Synthesis of activated carbon doped with transition metals for hydrogen storage*, 2019, DOI: 10.1051/e3sconf/20199001016.
38 S. R. Stoyanov, A. V. Titov and P. Král, *Coord. Chem. Rev.*, 2009, **253**, 2852–2871.
39 H. Feng, J. Ma and Z. Hu, *J. Mater. Chem.*, 2010, **20**, 1702–1708.
40 Y. Pan, Y. Liu, Y. Lin and C. Liu, *ACS Appl. Mater. Interfaces*, 2016, **8**, 13890–13901.
41 D. Paul, J. Deb, B. Bhattacharya and U. Sarkar, *Density functional theory study of pristine and transition metal doped fullerene*, 2017DOI: 10.1063/1.4980340.
42 S. Liu, F.-W. Gao, H.-L. Xu and Z.-M. Su, *Mol. Phys.*, 2019, **117**, 705–711.
43 M. K. Ubhi, M. Kaur, J. K. Grewal and V. K. Sharma, *Materials*, 2023, **16**, 1155.
44 L. Panchakarla, A. Govindaraj and C. Rao, *Inorg. Chim. Acta*, 2010, **363**, 4163–4174.
45 G. V. Kaliyannan, R. Rathanasamy, R. Gunasekaran, M. S. Anbupalani, M. Chinnasamy and S. K. Palaniappan, *Defect Engineering of Carbon Nanostructures*, 2022, pp. 83–109.
46 S. Ha, G. B. Choi, S. Hong, D. W. Kim and Y. A. Kim, *Carbon Lett.*, 2018, **27**, 1–11.
47 J. P. Paraknowitsch and A. Thomas, *Energy Environ. Sci.*, 2013, **6**, 2839–2855.
48 Y. Wang, L. Yu, W. Zhu, X. Zhou, Y. Chen and W. Peng, *Ionics*, 2019, **25**, 3499–3522.
49 A. L. M. Reddy, A. E. Tanur and G. C. Walker, *Int. J. Hydrogen Energy*, 2010, **35**, 4138–4143.
50 P. M. Revabhai, R. K. Singhal, H. Basu and S. K. Kailasa, *J. Nanostruct. Chem.*, 2023, **13**, 1–41.
51 D. V. Shtansky, A. T. Matveev, E. S. Permyakova, D. V. Leybo, A. S. Konopatsky and P. B. Sorokin, *Nanomaterials*, 2022, **12**, 2810.
52 N. De Sousa Sousa, A. L. P. Silva, A. C. A. Silva and J. de Jesus Gomes Varela Júnior, *J. Inorg. Organomet. Polym. Mater.*, 2024, **34**, 4082–4099.
53 M. Asif, M. H. S. A. Hamid, I. Bayach, N. S. Sheikh and K. Ayub, *Phys. Scr.*, 2024, **99**, 105522.
54 Q. Weng, L. Zeng, Z. Chen, Y. Han, K. Jiang, Y. Bando and D. Golberg, *Adv. Funct. Mater.*, 2021, **31**, 2007381.
55 S. A. Aal and A. K. Alfuhaidi, *Vacuum*, 2021, **183**, 109838.
56 S. Hu, Y. Yong, C. Li, Z. Zhao, H. Jia and Y. Kuang, *Phys. Chem. Chem. Phys.*, 2020, **22**, 13563–13568.
57 P. Banerjee, B. Pathak, R. Ahuja and G. Das, *Int. J. Hydrogen Energy*, 2016, **41**, 14437–14446.
58 S. Bhattacharya, C. Majumder and G. Das, *J. Phys. Chem. C*, 2009, **113**, 15783–15787.
59 X. Chen, X. Gao, H. Zhang, Z. Zhou, W. Hu, G. Pan, H. Zhu, T. Yan and D. Song, *J. Phys. Chem. B*, 2005, **109**, 11525–11529.
60 M. Chen, Y.-J. Zhao, J.-H. Liao and X.-B. Yang, *Phys. Rev. B: Condens. Matter Mater. Phys.*, 2012, **86**, 045459.
61 W. Rakrai, C. Tabtimsai, C. Kaewtong, S. Chuekachang, S. Keawwangchai, T. Keawwangchai and B. Wanno, *Struct. Chem.*, 2024, **35**, 437–453.
62 A. S. Rad and K. Ayub, *Int. J. Hydrogen Energy*, 2016, **41**, 22182–22191.
63 M. Frisch, *Gaussian 09, IOps Reference*, Gaussian, Inc, Wallingford CT, 2009, p. 201.
64 K. J. Kron, J. R. Hunt, J. M. Dawlaty and S. Mallikarjun Sharada, *J. Phys. Chem. A*, 2023, **127**, 1801–1802.
65 M. Gray, P. E. Bowling and J. M. Herbert, *J. Phys. Chem. A*, 2024, **128**, 7739–7745.
66 D. Padula, J. Cerezo, G. Pescitelli and F. Santoro, *Phys. Chem. Chem. Phys.*, 2017, **19**, 32349–32360.
67 B. Chan and G. E. Ball, *J. Chem. Theory Comput.*, 2013, **9**, 2199–2208.
68 S. Pan, G. Merino and L. Zhao, *Chemical Reactivity in Confined Systems: Theory, Modelling and Applications*, 2021, pp. 239–261.
69 A. Lashkaripour, W. Park, M. Mazaherifar and C. H. Choi, *J. Chem. Theory Comput.*, 2025, **21**, 5661–5668.
70 Q. Ren, S. Guan, F. Jiang and J. Fang, *J. Phys. Chem. A*, 2013, **117**, 756–764.
71 M. R. Provorse Long and C. M. Isborn, *J. Phys. Chem. B*, 2017, **121**, 10105–10117.
72 B. Mennucci, *Wiley Interdiscip. Rev.:Comput. Mol. Sci.*, 2012, **2**, 386–404.

73 W. Li, H. Xie, Y. Huang, L. Song, Y. Shao and K. Qiu, *J. Kunming Med. Univ.*, 2016, 134–136.
74 G. Zhurko and D. Zhurko, 2025, https://www.chemcraftprog.com.
75 W. Humphrey, A. Dalke and K. Schulten, *J. Mol. Graphics*, 1996, **14**, 33–38.
76 T. Lu and F. Chen, *J. Comput. Chem.*, 2012, **33**, 580–592.
77 E. Lindahl, B. Hess and D. Van Der Spoel, *Mol. Model. Annu.*, 2001, **7**, 306–317.
78 R. Briones, C. Blau, C. Kutzner, B. L. de Groot and C. Aponte-Santamaría, *Biophys. J.*, 2019, **116**, 4–11.
79 L. Kagami, A. Wilter, A. Diaz and W. Vranken, *Bioinformatics*, 2023, **39**, btad350.
80 A. W. Sousa da Silva and W. F. Vranken, *BMC Res. Notes*, 2012, **5**, 367.
81 B. Hess, H. Bekker, H. J. Berendsen and J. G. Fraaije, *J. Comput. Chem.*, 1997, **18**, 1463–1472.
82 R. E. Isele-Holder, W. Mitchell and A. E. Ismail, *J. Chem. Phys.*, 2012, **137**, 174107.
83 M. Noormohammadbeigi, S. Kamalinahad, F. Izadi, M. Adimi and A. Ghasemkhani, *Mater. Res. Express*, 2020, **6**, 1250g1252.
84 N. de Sousa Sousa and J. de Jesus Gomes Varela Junior, *Langmuir*, 2025, **41**, 7396–7409.
85 Y. Arshad, M. Asghar, M. Yar, T. Bibi and K. Ayub, *J. Inorg. Organomet. Polym. Mater.*, 2023, **33**, 943–955.
86 W. McKenzie, D. Batani, T. A. Mehlhorn, D. Margarone, F. Belloni, E. M. Campbell, S. Woodruff, J. Kirchhoff, A. Paterson and S. Pikuz, *J. Fusion Energy*, 2023, **42**, 17.
87 M. Ghara, S. Pan and P. K. Chattaraj, *Phys. Chem. Chem. Phys.*, 2019, **21**, 21267–21277.
88 T. Anusuya and V. Kumar, *Phys. Chem. Chem. Phys.*, 2022, **25**, 262–273.
89 P. E. Hoggan, in *Advances in Quantum Chemistry*, Elsevier, 2018, vol. 76, pp. 271–278.
90 M. Wijzenbroek, D. Helstone, J. Meyer and G.-J. Kroes, *J. Chem. Phys.*, 2016, **145**, 144701.
91 A. Montoya, A. Schlunke and B. S. Haynes, *J. Phys. Chem. B*, 2006, **110**, 17145–17154.
92 I. Bayach, S. Sarfaraz, N. S. Sheikh, K. Alamer, N. Almutlaq and K. Ayub, *Materials*, 2023, **16**, 2792.
93 A. B. Shah, S. Sarfaraz, M. Yar, N. S. Sheikh, H. H. Hammud and K. Ayub, *Nanomaterials*, 2022, **13**, 29.
94 Z. Zhang, X. Zhou, C. Liu, J. Guo and H. Ning, *Int. J. Hydrogen Energy*, 2018, **43**, 793–800.
95 R. Trivedi and D. Bandyopadhyay, *Int. J. Hydrogen Energy*, 2016, **41**, 20113–20121.
96 M. Pozzo, *arXiv*, 2008, preprint, arXiv:0811.3313, DOI: 10.48550/arXiv:0811.3313.
97 X. Yu, Y. Tong and Y. Yang, *Chin. Phys. B*, 2023, **32**, 108103.
98 N. S. Venkataramanan, A. Suvitha and Y. Kawazoe, *J. Mol. Liq.*, 2018, **260**, 18–29.
99 M. Nishat, M. R. Hossain, M. M. Hasan, M. K. Hossain, M. A. Hossain and F. Ahmed, *J. Biomol. Struct. Dyn.*, 2023, **41**, 3413–3429.
100 A. D. Tamafo Fouégué, H. Tendongmo, E. Sakué Ngankam and R. Abdoul Ntieche, *J. Biomol. Struct. Dyn.*, 2023, **41**, 9721–9731.
101 V. de Paul Zoua, F. K. Bine, I. F. Pagoré, A. D. T. Fouegue and R. A. Ntieche, *Comput. Theor. Chem.*, 2024, **1240**, 114807.